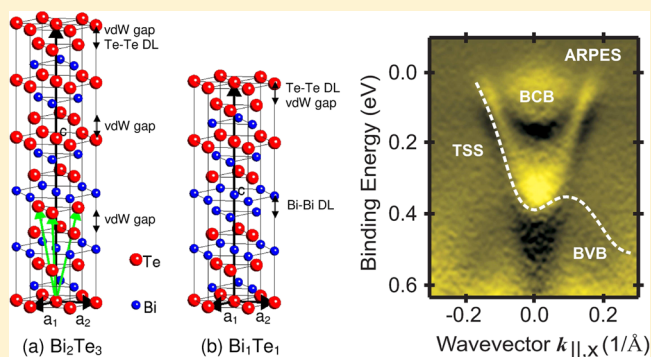


Growth, Structure, and Electronic Properties of Epitaxial Bismuth Telluride Topological Insulator Films on BaF<sub>2</sub> (111) SubstratesO. Caha,<sup>†</sup> A. Dubroka,<sup>†</sup> J. Humlíček,<sup>†</sup> V. Holý,<sup>‡</sup> H. Steiner,<sup>§</sup> M. Ul-Hassan,<sup>§</sup> J. Sánchez-Barriga,<sup>||</sup> O. Rader,<sup>||</sup> T. N. Stanislavchuk,<sup>⊥</sup> A. A. Sirenko,<sup>⊥</sup> G. Bauer,<sup>§</sup> and G. Springholz<sup>\*,§</sup><sup>†</sup>Department of Condensed Matter Physics and CEITEC, Masaryk University, Kotlářská 2, 61137 Brno, Czech Republic<sup>‡</sup>Department of Electronic Structures, Charles University, Praha, Czech Republic<sup>§</sup>Institut für Halbleiter- und Festkörperphysik, Johannes Kepler Universität, Altenbergerstrasse 69, 4040 Linz, Austria<sup>||</sup>Helmholtz-Zentrum Berlin für Materialien und Energie, Elektronenspeicherring BESSY II, Albert-Einstein-Straße 15, 12489 Berlin, Germany<sup>⊥</sup>Department of Physics, New Jersey Institute of Technology, Newark, New Jersey 07102, United States

## S Supporting Information

**ABSTRACT:** Epitaxial growth of topological insulator bismuth telluride by molecular beam epitaxy onto BaF<sub>2</sub> (111) substrates is studied using Bi<sub>2</sub>Te<sub>3</sub> and Te as source materials. By changing the beam flux composition, different stoichiometric phases are obtained, resulting in high quality Bi<sub>2</sub>Te<sub>3</sub> and Bi<sub>1</sub>Te<sub>1</sub> epilayers as shown by Raman spectroscopy and high-resolution X-ray diffraction. From X-ray reciprocal space mapping, the residual strain, as well as size of coherently scattering domains are deduced. The Raman modes for the two different phases are identified and the dielectric functions derived from spectroscopic ellipsometry investigations. Angular resolved photoemission reveals topologically protected surface states of the Bi<sub>2</sub>Te<sub>3</sub> epilayers. Thus, BaF<sub>2</sub> is a perfectly suited substrate material for the bismuth telluride compounds.



## ■ INTRODUCTION

Recent discovery of a new class of materials, called topological insulators, has opened up a whole new research arena.<sup>1–5</sup> Topological insulators behave in the bulk like ordinary insulators but support in addition a conducting two-dimensional topological surface state with linear energy-momentum dispersion shaped like a Dirac cone.<sup>2,6,7</sup> Because of strong spin-orbit coupling, the electron momentum in these surface states is locked to the spin orientation and spin-flip scattering is prohibited by time reversal symmetry.<sup>1,8</sup> As a result, spin polarized currents can be produced without the needs of external magnetic fields, which offers great advantages for spintronic or quantum computation applications.<sup>1,5,9</sup> The helical spin structure of the topological surface states also provides a basis for fundamental new physics such as magnetic monopoles and Majorana fermions.<sup>1,2</sup>

Among the new materials exhibiting three-dimensional topological insulating properties, the bismuth chalcogenides Bi<sub>2</sub>Te<sub>3</sub> and Bi<sub>2</sub>Se<sub>3</sub> have attracted most attention because a single Dirac cone is formed at the  $\Gamma$ -point of the Brillouin zone within the bulk band gap, as has been revealed by angular resolved photoemission<sup>8,7</sup> and scanning tunneling spectroscopy studies.<sup>10,11</sup> Bi<sub>2</sub>Te<sub>3</sub> is also a superior thermoelectric material for energy harvesting applications, since it exhibits the highest

thermoelectric figure of merit at room temperature among all bulk materials.<sup>12,13</sup> Up to now, most studies of the topological properties of Bi<sub>2</sub>Te<sub>3</sub> have been performed on bulk single crystals cleaved under ultrahigh vacuum conditions.<sup>3,7,14</sup> For practical device applications, however, epitaxial layers are desired<sup>15</sup> for monolithic integration in multilayers and gated heterostructures that would allow tuning of the Fermi level to the Dirac point and control spin polarized currents in devices.<sup>15,16</sup> Considerable efforts have been made to grow Bi<sub>2</sub>Te<sub>3</sub> epitaxially on substrates like Si<sup>17–21</sup> or GaAs,<sup>22–26</sup> which, however, exhibit a very large lattice mismatch of up to 14% to Bi<sub>2</sub>Te<sub>3</sub>.

Bismuth telluride can crystallize in several different crystal structures in dependence of its stoichiometric composition. The crystal structure of the most common Bi<sub>2</sub>Te<sub>3</sub> phase consists of three Te<sup>1</sup>–Bi–Te<sup>2</sup>–Bi–Te<sup>1</sup> quintuplet layers (QL) as fundamental building block (see Figure 1a). These are stacked on top of each other in an ABCABC stacking sequence. In addition, several alternative phases with lower Te concentration exist, including Bi<sub>1</sub>Te<sub>1</sub> (called tsumoite), as well as Bi<sub>3</sub>Te<sub>4</sub> and

Received: January 9, 2013

Revised: May 15, 2013

Published: July 12, 2013

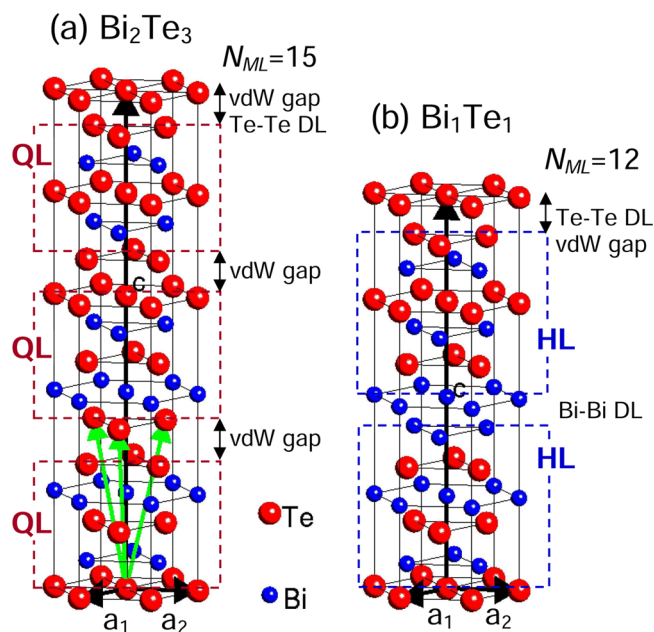


**Figure 1.** Hexagonal unit cell of (a)  $\text{Bi}_2\text{Te}_3$  and (b)  $\text{BiTe}$  with the base vectors indicated by the black arrows. For  $\text{Bi}_2\text{Te}_3$ , the unit cell consists of 15 atomic lattice planes that are grouped in three quintuple layers (QL) with  $\text{Te}^1\text{-Bi-Te}^2\text{-Bi-Te}^1$  stacking. The quintuple layers are van der Waals bonded to each other by a  $\text{Te-Te}$  double layer (van der Waals gap). For  $\text{BiTe}$ , the unit cell consists of 12 atomic lattice planes with  $\text{Te}^1\text{-Bi}^1\text{-Te}^2\text{-Bi}^2\text{-Te}^3\text{-Bi}^3\text{-Bi}^3\text{-Te}^3\text{-Bi}^2\text{-Te}^2\text{-Bi}^1\text{-Te}^1$  stacking sequence that can be split in two hexuple layer (HL) blocks. The green arrows indicate an alternative definition of the crystal structure using rhombohedral base vectors. The lattice parameters of  $\text{Bi}_2\text{Te}_3$  and  $\text{BiTe}$  are listed in Table 1.

$\text{Bi}_4\text{Te}_3$  (pilsenite) among others.<sup>27</sup> The different phases share the same hexagonal structure of  $R\bar{3}m$  space group symmetry, but show a different stacking of the Bi and Te layers.<sup>28,29</sup> The  $\text{Bi}_1\text{Te}_1$  structure, depicted in Figure 1b, consists of twelve atomic  $\text{Te}^1\text{-Bi}^1\text{-Te}^2\text{-Bi}^2\text{-Te}^3\text{-Bi}^3\text{-Bi}^3\text{-Te}^3\text{-Bi}^2\text{-Te}^2\text{-Bi}^1\text{-Te}^1$  lattice planes<sup>30</sup> that can be split into two mirrored hexuple layers (HL). The unit cells of  $\text{Bi}_4\text{Te}_3$  and  $\text{Bi}_3\text{Te}_4$  consist even of 21 lattice planes grouped in three blocks of septuplet layers, comprising each of seven lattice planes. While  $\text{Bi}_2\text{Te}_3$  has been intensely studied over the past few years, the properties of the other phases have remained rather unexplored. In particular,

$\text{BiTe}$  has been available only in the form of bulk crystals<sup>30</sup> or polycrystalline films,<sup>31</sup> that is, to the best of our knowledge no work on epitaxial  $\text{BiTe}$  layers has been published so far.

In the present work, we report on molecular beam epitaxy (MBE) of single phase  $\text{Bi}_2\text{Te}_3$  and  $\text{BiTe}$  epilayers and we provide detailed insight in their structural and electronic properties. Contrary to most previous studies, epitaxial growth is carried out on  $\text{BaF}_2$  (111) substrates,<sup>32</sup> which exhibit an almost perfect matching of the in-plane lattice constant to those of the bismuth telluride compounds (see Table 1). In fact, the lattice-misfit to  $\text{Bi}_2\text{Te}_3$  of  $\Delta a_{\parallel}/a = 0.04\%$  is particularly small, that is,  $\text{BaF}_2$  is practically lattice-matched.  $\text{BaF}_2$  also features several additional advantages. First of all,  $\text{BaF}_2$  is highly insulating and optically transparent, which is favorable for transport measurements and optical spectroscopy. Second, because of the perfect (111) orientation, cleaved  $\text{BaF}_2$  substrates are virtually step free over tens of square micrometer surface areas, contrary to the usual miscut steps with spacing smaller than 100 nm present on standard Si or GaAs substrate surfaces. As the lattice plane stacking and the height of these steps differs from those of the bismuth tellurides, these steps act as sources for stacking faults and antiphase domain boundaries in epilayers.  $\text{BaF}_2$  also shows a better matching of the in-plane thermal expansion coefficient of  $18.7 \times 10^{-6} \text{ K}^{-1}$  to that of  $\text{Bi}_2\text{Te}_3$  of  $14 \times 10^{-6} \text{ K}^{-1}$  at 300 K<sup>33</sup> compared to Si ( $2.6 \times 10^{-6} \text{ K}^{-1}$ ) or GaAs ( $5.73 \times 10^{-6} \text{ K}^{-1}$ ). As shown in this work, this leads to rather low values of thermal stress within the epilayers. The thermal expansion coefficient of bulk  $\text{BiTe}$  has not been reported so far, but one can assume that it is similar to that of  $\text{Bi}_2\text{Te}_3$ .

In terms of growth, we show that by tuning of the beam flux composition, that is, the tellurium to bismuth flux ratio, single phase  $\text{Bi}_2\text{Te}_3$  and  $\text{BiTe}$  epilayers are obtained. Their excellent structural perfection is demonstrated by high resolution X-ray diffraction and the optimum growth conditions for the different phases are derived. Quantitative evaluation of reciprocal space maps yields the strain as well as size of coherently scattering domains and by Raman scattering the active phonons in both compounds are identified. Raman experiments carried out in backscattering geometry from the surface as well as from the layer/substrate interface show that the entire epilayers are single phase even for thicknesses as large as 830 nm. By infrared and far-infrared spectroscopy we determine the plasma frequencies and thus, the free carrier concentrations of the

**Table 1.** Structural Properties of the  $\text{BiTe}$  and  $\text{Bi}_2\text{Te}_3$  Epilayers Grown on  $\text{BaF}_2$  (111) Substrates Determined by X-ray Reciprocal Space Mapping Compared to Results for Bulk Materials Reported in Literature<sup>a</sup>

composition	sample	$d$ (nm)	$a$ (Å)	$c$ (Å)	$R_L$ (nm)	$R_V$ (nm)	$\Delta\phi$ (deg)
$\text{Bi}_2\text{Te}_3$ -epilayers	M2780	830	4.3804	30.53	6000	200	0.08
	M2704	250	4.382	30.51	1300	80	0.05
$\text{Bi}_2\text{Te}_3$ -bulk	ref 34		4.3835	30.487			
	ref 35		4.386	30.497			
	ref 36		4.3852	30.483			
$\text{BiTe}$ -epilayers	M2777	400	4.402	24.202	200	40	0.18
	M2732	250	4.400	24.229	100	40	0.2
$\text{BiTe}$ -bulk	ref 30		4.423	24.002			
	ref 37		4.422	24.052			
	ref 38		4.40	23.97			
$\text{BaF}_2$ (111)	ref 39		4.384	10.739			

<sup>a</sup>Also listed are the in- and out-of-plane lattice constant of the (111)  $\text{BaF}_2$  substrates, with cubic lattice constants of  $a_0 = 6.200 \text{ Å}$ . The average lateral and vertical mosaic block sizes  $R_{L,V}$  and the root mean square angular lattice misorientation  $\Delta\phi$  of the epilayers were obtained from Figure 4.

layers. By angular resolved photoemission, the surface band structure of the  $\text{Bi}_2\text{Te}_3$  epilayers is established, showing a well-resolved Dirac cone with pronounced hexagonal warping. Thus, these layers are very well suited for further studies of the topological properties of this material.

## EXPERIMENTAL SECTION

Bismuth telluride epilayers were grown by molecular beam epitaxy in a Riber 1000 system under ultrahigh vacuum conditions at a background pressure of  $5 \times 10^{-10}$  mbar. The molecular beams were generated using a compound bismuth telluride effusion cell (nominal composition of  $\text{Bi}_2\text{Te}_3$ ) operated at around 500 °C, and a separate tellurium cell operated at 280–330 °C for stoichiometry control. The flux rates were 1–2 Å/s for bismuth telluride and 0–2 Å/s for excess tellurium, which was controlled by a quartz crystal microbalance. The layers were deposited on cleaved  $\text{BaF}_2$  (111) substrates at substrate temperatures between 300–400 °C measured with an infrared optical pyrometer. The surface structure of the films was monitored by in situ reflection high-energy electron diffraction as well as atomic force microscopy (AFM). X-ray diffraction experiments were performed using a high-resolution X-ray diffractometer equipped with a Cu tube, parabolic mirror and four-bounce Ge (220) Bartels monochromator on the primary side, and a channel-cut Ge (220) analyzer on the secondary side. Unpolarized Raman spectra were acquired with a Renishaw InVia spectrometer at room temperature in backscattering geometry. The exciting beam of a 632.8 nm HeNe laser was focused either on the front side surface or backside of the films through the transparent  $\text{BaF}_2$  substrate. The spot size was about 2  $\mu\text{m}$  and the laser power was low enough to avoid local heating.

The optical properties were determined by ellipsometric measurements using a home-built ellipsometer attached to a Bruker IFSS5 EQUINOX mid-infrared Fourier spectrometer. In the near-infrared, visible, and ultraviolet range, ellipsometric spectra were acquired with a Woollam M-2000 and Jobin Yvon UVISSEL ellipsometer. This was complemented by reflectance measurements in the 0.01–0.2 eV range using a Bruker IFS 66v/S spectrometer as well as far-infrared ellipsometric measurements at the NLS synchrotron light source in Brookhaven. The Hall conductivity was determined by van der Pauw measurements. The electronic structure was determined by angle resolved photoemission spectroscopy (ARPES) at the UE112-PGM2a beamline of BESSY II, Berlin using a Scienta R8000 electron analyzer and linearly polarized light with 21 eV photon energy. For these measurements, the epilayers were protected after growth by a Te capping layer deposited in the MBE system. This layer was desorbed in the ultrahigh vacuum ARPES chamber just before the photoemission experiments.

## RESULTS AND DISCUSSION

**Molecular Beam Epitaxy.** Epitaxial growth of bismuth telluride onto (111)  $\text{BaF}_2$  substrates proceeds in a 2D growth mode at substrate temperatures above 300 °C independent of the beam flux composition, i.e., independent of the excess Te flux. This is evidenced by the streaked RHEED diffraction patterns observed during growth presented in Figure 2 for two samples grown with a Te flux of (a) 2 and (b) 0 Å/s, respectively. At substrate temperatures below 300 °C, a significant roughening of the surface due to limited surface diffusion occurs. For high excess Te flux greater than 2 Å/s, which is a factor of 2 larger compared to the bismuth telluride flux, the stoichiometric composition of the epilayers corresponds to  $\text{Bi}_2\text{Te}_3$  as proven by the X-ray analysis described below. Without or with only very small excess Te flux, the Te content of the epilayers is reduced such that more Bi rich epilayers are formed with a stoichiometry close to the  $\text{Bi}_1\text{Te}_1$  phase. For both types of samples, atomic force microscopy measurements reveal smooth, that is, atomically flat surfaces as

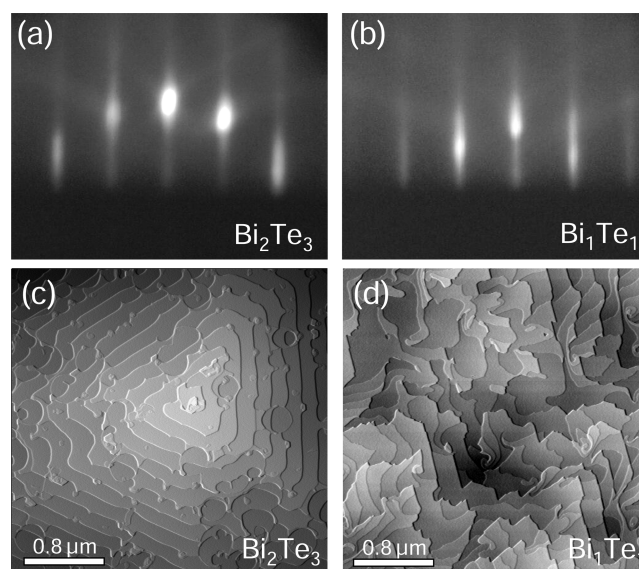


**Figure 2.** Reflection high-energy electron diffraction patterns observed in situ during molecular beam epitaxy of (a)  $\text{Bi}_2\text{Te}_3$  and (b)  $\text{Bi}_1\text{Te}_1$  along the  $[1\bar{1}00]$  azimuth direction. Corresponding atomic force microscopy surface images of 400 nm thick epilayers are shown in panels c and d, respectively. The growth conditions differ only in the excess Te flux supplied during growth of 2 and 0 Å/s for panels a and c and panels b and d, respectively. The substrate temperature was 350 °C.

shown by Figure 2c and d, respectively. On the  $\text{Bi}_2\text{Te}_3$  layers, surface steps of predominantly one quintuple unit thickness, that is, 10.1 Å height, are found, meaning that the surface is tellurium terminated at the van der Waals gaps, in agreement with previous studies.<sup>40</sup> For the  $\text{BiTe}$  layers, a broader variation of step heights from 4 Å corresponding to single  $\text{BiTe}$  bilayers, up to 24 Å equivalent to the 12 atomic layers of the hexagonal unit cell are observed. This arises from the fact that the unit cell of  $\text{BiTe}$  includes only one weakly bonded van der Waals Te–Te double layer (DL), that is repeated only every 12 atomic lattice planes (see Figure 1b). On a 10  $\mu\text{m}$  length scale, the root-mean-square roughness of the epilayers is less than a few nm in both cases.

Apart from single phase  $\text{Bi}_2\text{Te}_3$  and  $\text{BiTe}$  layers obtained with high, respectively, low excess Te flux, epilayers with mixed bismuth telluride phases are formed at intermediate Te flux rates. These layers show multiple X-ray diffraction peaks arising from several bismuth telluride phases and were not considered for further analysis. The RHEED patterns of these layers, however, are almost indistinguishable from those of the single phase layers as the different bismuth telluride phases differ only in their Bi–Te layer stacking sequence, whereas the overall hexagonal in-plane lattice structure and lattice constant is nearly preserved.<sup>27</sup> The AFM images of such layers exhibit a broader range of step heights because of the variation of the vertical lattice plane stacking of the different regions. This indicates that the coexistence of the different phases is mainly accommodated by stacking faults in the layers. In order to study and compare in detail the structural and electronic properties of the two main bismuth telluride phases, only single phase epilayers consisting of pure  $\text{BiTe}$  and  $\text{Bi}_2\text{Te}_3$  were employed for further analysis. The corresponding sample parameters are indicated in Table 1 and the layer thicknesses ranged from 250 to 830 nm.

**Structure Analysis.** The crystal structures of the bismuth tellurides with the  $R\bar{3}m$  space group can be described by two

equivalent definitions of the base vectors in rhombohedral or hexagonal axes, as indicated by the black and green arrows in Figure 1, respectively. In this paper, we use the hexagonal definition of the base vectors  $a$  and  $c$  perpendicular, respectively, parallel to the hexagonally ordered atomic (Te,Bi) planes, where the  $c$ -axis is equivalent to the [0001] hexagonal or [111] rhombohedral direction. As illustrated by Figure 1, the structures of  $\text{Bi}_2\text{Te}_3$  and BiTe mainly differ by their different stacking sequence. For  $\text{Bi}_2\text{Te}_3$ , the hexagonal unit cell consists of three quintuple layers, that is, five atomic  $\text{Te}^1\text{-Bi-Te}^2\text{-Bi-Te}^2$  planes stacked on top of each other, corresponding in total to 15 lattice planes per unit cell. The quintuple layers are weakly bonded together by van der Waals forces between the Te-Te double layer, for which the lattice plane spacing is increased by  $\sim 36\%$  compared to the average value of  $2.032 \text{ \AA} = c/15$ . The unit cell of BiTe consists of a single block of twelve atomic planes with  $\text{Te}^1\text{-Bi}^1\text{-Te}^2\text{-Bi}^2\text{-Te}^3\text{-Bi}^3\text{-Bi}^3\text{-Te}^3\text{-Bi}^2\text{-Te}^2\text{-Bi}^1\text{-Te}^1$  stacking sequence.<sup>30</sup> As shown by Figure 1, it contains only one weakly bonded Te-Te van der Waals double layer, but an additional metallic Bi-Bi double layer in the middle of the cell that joins together two hexuplet layers with inverse stacking sequence. The nominal lattice parameters of  $\text{Bi}_2\text{Te}_3$  are  $a = 4.384 \text{ \AA}$  and  $c = 30.487 \text{ \AA}$ ,<sup>34-36</sup> and for BiTe, they are around  $4.423$  and  $24.002 \text{ \AA}$  with some variation in literature<sup>30,37,38</sup> (see Table 1). Thus, the in-plane atomic distances in BiTe are slightly larger and the average vertical lattice-plane spacing slightly smaller compared to  $\text{Bi}_2\text{Te}_3$ . For both compounds, the in-plane hexagonal lattice parameter  $a$  fits well to the in-plane lattice constant  $a_{\parallel} = 4.384 \text{ \AA} = a_0/\sqrt{2}$  of (111)  $\text{BaF}_2$  substrates. In fact,  $\text{Bi}_2\text{Te}_3$  is practically lattice matched to  $\text{BaF}_2$  with a lattice misfit  $\Delta a_{\parallel}/a < 0.04\%$ . For BiTe, the lattice-mismatch is somewhat larger, but it is still less than  $0.9\%$ , depending on the used bulk lattice parameter.

Phase analysis of the samples was assessed using X-ray diffraction along the symmetric truncation rod perpendicular to the epilayer surface. The resulting diffraction curves of  $\text{Bi}_2\text{Te}_3$  and BiTe epilayers are presented in Figure 3 in red and blue

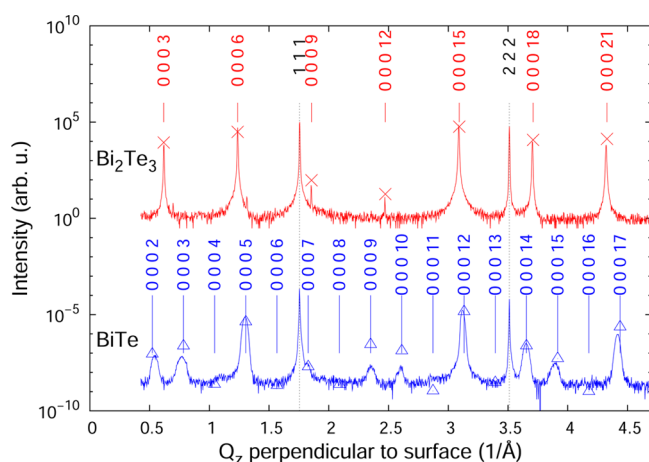


**Figure 3.** Symmetric X-ray diffraction scans along  $q_z$  perpendicular to the surface of  $\text{Bi}_2\text{Te}_3$  (red line, sample M2780) and BiTe (blue line, sample M2777) epilayers grown on  $\text{BaF}_2$  (111) substrates. The vertical lines denote the calculated ( $hkl$ ) Bragg positions of the layer and substrate peaks, and the crosses and diamonds the intensity, that is, structure factors computed for the  $\text{Bi}_2\text{Te}_3$ , respectively, BiTe lattice structures shown in Figure 1. The sample parameters are listed in Table 1.

color, respectively. Evidently, the layers show only the (000 $l$ ) Bragg peaks of  $\text{Bi}_2\text{Te}_3$  and BiTe as indicated by the vertical red and blue lines. Thus, the layers grow in  $c$ -axis orientation on the  $\text{BaF}_2$  substrates for which the (111) and (222) peaks are indicated by the black dotted lines. For  $\text{Bi}_2\text{Te}_3$ , because of the 3-fold quintuple layer stacking, only the Bragg peaks with  $l = 3, 6, 9, 12, \dots$  appear in the diffraction spectra, whereas no such simple selection rule exists for BiTe due to its twelve atomic layer stacking. As indicated by the crosses and triangles, for both samples the positions and intensities of the diffraction peaks correspond very well to the calculated values, and no other secondary phases are observed. This demonstrates that by appropriate choice of the MBE growth conditions single phase epilayers can be obtained.

Detailed structural information of the epilayers were derived by X-ray diffraction reciprocal-space mapping.<sup>41</sup> In this technique, the diffusely scattered intensity is measured as a function of the scattering vector  $\mathbf{Q} = \mathbf{K}_{\text{final}} - \mathbf{K}_{\text{incident}}$  in the vicinity of various reciprocal-lattice vectors  $\mathbf{h}$  (diffraction vector). For a structurally perfect layer, the reciprocal-space map (RSM) consists of a narrow vertical rod of lateral width  $\Delta Q_x$  determined only by the experimental resolution. Its width along  $Q_z$  is inversely proportional to the layer thickness  $d$  according to  $\Delta Q_z \approx 2\pi/d$ . On the contrary, a layer with structural defects produces a broader RSM maximum, the shape of which depends on the nature and density of defects whereas its position depends on the composition and strain state of the layer.

For all samples, reciprocal space maps were recorded around the symmetric and asymmetric reciprocal lattice points (RLP)  $\mathbf{h}_{\text{sym}} = (00012)$  and  $\mathbf{h}_{\text{asym}} = (1\bar{1}016)$  for BiTe and  $\mathbf{h}_{\text{sym}} = (00015)$  and  $\mathbf{h}_{\text{asym}} = (1\bar{1}020)$  for  $\text{Bi}_2\text{Te}_3$ . The results are presented in Figure 4a–d, respectively. For the two phases, the chosen RLPs are approximately at the same positions in

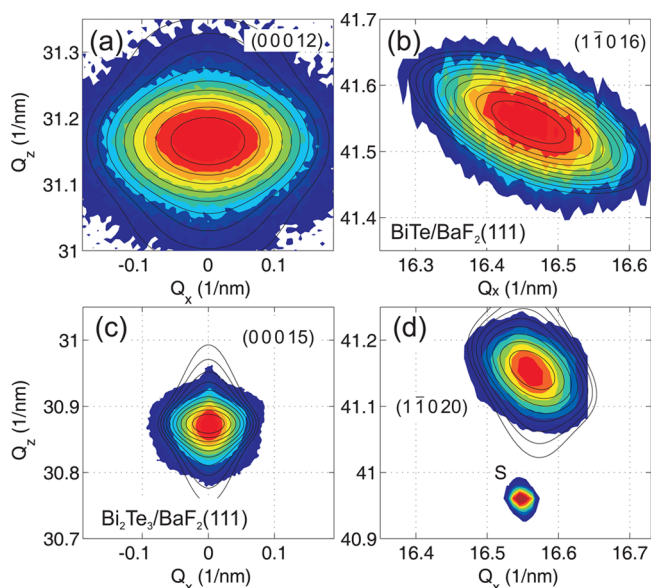


**Figure 4.** Reciprocal space maps of the 400 nm BiTe epilayer M2777 (top) and 800 nm  $\text{Bi}_2\text{Te}_3$  epilayer M2780 (bottom) on  $\text{BaF}_2$  (111), measured around the symmetric (00012) (a) and (00015) (c) as well as asymmetric ( $1\bar{1}016$ ) (b) and ( $1\bar{1}020$ ) (d) reciprocal lattice points. The simulation of the measured intensity distributions using a mosaic-block model is represented by the black contour lines and the resulting structure parameters are listed in Table 1.

reciprocal space, which allows a direct comparison of the scattered intensity distributions. Evidently the intensity distribution is considerably broader for the BiTe compared to the Bi<sub>2</sub>Te<sub>3</sub> epilayer, but in both cases the widths are larger than for a perfect epilayer. For the BiTe layer (upper part of Figure 4) the vertical and lateral full width at half-maximum (fwhm) is  $\Delta Q_x = 0.1299 \text{ nm}^{-1}$  and  $\Delta Q_z = 0.0823 \text{ nm}^{-1}$ , respectively, and for the Bi<sub>2</sub>Te<sub>3</sub> layer (lower part of Figure 4)  $\Delta Q_x = 0.0328 \text{ nm}^{-1}$  and  $\Delta Q_z = 0.0397 \text{ nm}^{-1}$ . To account for this broadening, the defect structure was approximated by a mosaic model in which the layers consist of randomly placed and randomly rotated coherent domains (mosaic blocks).<sup>41,42</sup> For simulation of the reciprocal space maps, the coherent domains are assumed as uniaxial ellipsoids with mean lateral and vertical radii  $R_L$  and  $R_V$ , respectively, and root-mean square (rms) angular lattice misorientations  $\Delta\phi$ . The domain size is random and the radii are distributed according to the Gamma distribution with order  $m_R$ , so that the rms deviations of the radii are  $\sigma_{L,R} = R_{L,V}/\sqrt{m_R}$ .

The calculated reciprocal space maps for both samples are represented as solid iso-intensity contour lines in Figure 4 that are superimposed on the measured data and the best fit structure parameters are listed in Table 1. Evidently, the simulations are in nice agreement with both the symmetric and asymmetric RSMs for both phases. For the BiTe layer, the mosaic block parameters are derived as  $R_L = (200 \pm 10) \text{ nm}$ ,  $R_V = (40 \pm 5) \text{ nm}$ , and  $\Delta\phi = (0.18 \pm 0.02)^\circ$ . The simulations are not much sensitive to the order  $m_R$  in the range between 5 and 20. We have performed a similar analysis also on the thinner  $d = 250 \text{ nm}$  BiTe layer and the resulting parameters are  $R_L = (100 \pm 10) \text{ nm}$ ,  $R_V = (40 \pm 5) \text{ nm}$ , and  $\Delta\phi = (0.20 \pm 0.02)^\circ$  as listed in Table 1. The values are very similar for both samples except for the lateral size of coherent domains, which in both cases roughly equals half of the layer thickness, whereas the lattice misorientations  $\Delta\phi$  and vertical coherent domain size  $R_V$  are independent of thickness. From the fit of the diffraction maxima, we obtain the BiTe lattice parameters as  $a = (4.401 \pm 0.002) \text{ \AA}$  and  $c = (24.21 \pm 0.01) \text{ \AA}$ , which are identical for both samples within the experimental precision. The lattice parameters differ somewhat from the bulk values listed in Table 1. This may arise from a residual epitaxial strain in the epilayers due to the nominal 0.9% mismatch to the BaF<sub>2</sub> substrate. However, given the uncertainty in the bulk lattice parameters, this could also be due to a deviation from the exact stoichiometric composition that also influences the lattice parameters.<sup>29</sup>

The same analysis was performed for the Bi<sub>2</sub>Te<sub>3</sub> samples. The resulting fit of the symmetric and asymmetric RSMs are displayed in Figure 4c and d, which yields a mean vertical and lateral radius of coherent domains of  $R_V = (100 \pm 30) \text{ nm}$  and  $R_L \approx (6000 \pm 200) \text{ nm}$ , where the latter exceeds the  $\sim 1 \mu\text{m}$  coherence width of the primary X-ray beam. The rms domain misorientation of  $\Delta\phi = (0.08 \pm 0.02)^\circ$  is significantly smaller than for the BiTe epilayers, and the same result was also found for the thinner 250 nm Bi<sub>2</sub>Te<sub>3</sub> layer (see Table 1) with domain radii of  $R_L = (130 \pm 50) \text{ nm}$  and  $R_V = (80 \pm 30) \text{ nm}$  and an rms misorientation of  $\Delta\phi = (0.05 \pm 0.03)^\circ$ . This evidences a higher structural perfection of the Bi<sub>2</sub>Te<sub>3</sub> layers resulting from the almost perfect lattice matching to the BaF<sub>2</sub> substrates. Similar results were recently obtained for Bi<sub>2</sub>Se<sub>3</sub>,<sup>43,44</sup> where a significant improvement of the structural quality was found for growth on nearly lattice matched InP (111) substrates compared to Si (111).

From the fit of the RSMs, the lattice parameters of the Bi<sub>2</sub>Te<sub>3</sub> epilayers were determined as  $a = (4.380 \pm 0.001) \text{ \AA}$  and  $c = (30.53 \pm 0.01) \text{ \AA}$ , which are identical to the bulk values (see Table 1) with a deviation of less than  $-0.08\%$ , respectively,  $+0.14\%$ . Essentially the same was also obtained for the thinner epilayer. Considering the bulk lattice constant of  $a = 4.3835 \text{ \AA}$  reported by Wyckoff,<sup>34</sup> a minute residual in-plane strain of  $-0.08\%$  is inferred in the epilayers, corresponding to an in-plane stress of  $\sim 40 \text{ MPa}$  using the elastic coefficients of Jenkins et al.<sup>45</sup> The ratio between the in-plane and out-of-plane strain values also agrees with the reported Poisson's ratio of Bi<sub>2</sub>Te<sub>3</sub>.<sup>45</sup> It is noted that the residual strain has actually the opposite sign of the  $+0.04\%$  layer/substrate lattice mismatch. This can be explained by the thermal expansion coefficient mismatch between BaF<sub>2</sub> and Bi<sub>2</sub>Te<sub>3</sub> of  $18.7 \times 10^{-6} \text{ K}^{-1}$  versus  $14 \times 10^{-6} \text{ K}^{-1}$ , which induces a small compressive in-plane strain of  $-0.15\%$  in the layers upon cooling from 350 °C to room temperature after growth. For thin Bi<sub>2</sub>Te<sub>3</sub> epilayers on Si (111) a significantly larger out-of-plane strain value of  $-1\%$  was recently reported.<sup>21</sup>

The epitaxial relationship of the samples was determined by azimuthal scans at the asymmetric  $(1\bar{1}016)$  and  $(1\bar{1}020)$  reciprocal lattice points of Bi<sub>2</sub>Te<sub>3</sub>, respectively, BiTe, where the samples were rotated around the surface normal vector at fixed X-ray incidence and exit angles. The results are displayed in Figure 5, where the azimuth angle  $\phi$  is measured relative to the

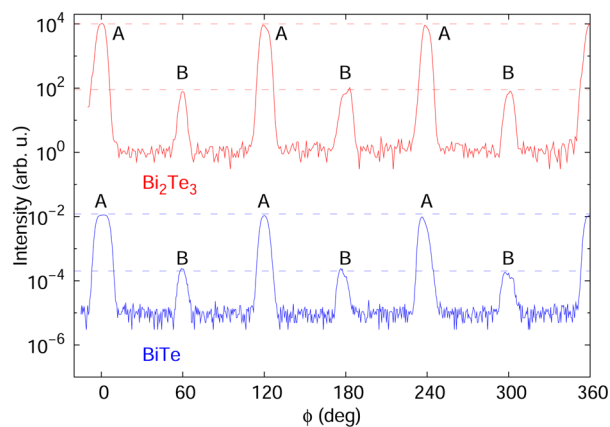


**Figure 5.** Azimuthal diffraction scans in the asymmetric diffraction maxima at  $h = (1\bar{1}020)$  for the Bi<sub>2</sub>Te<sub>3</sub> epilayer (upper curve) and at  $h = (1\bar{1}016)$  for the BiTe layer (lower curve) on BaF<sub>2</sub> (111) substrates. The azimuthal angle  $\phi$  is measured relative to the in-plane  $[1\bar{1}\bar{2}]$  substrate direction. The major peaks in the positions  $\phi = 0^\circ$ ,  $120^\circ$ , and  $240^\circ$  denoted by “A” correspond to the 3-fold symmetry along the  $c$ -axis with alignment of the  $[1\bar{1}00]$  crystallographic direction of the layer to the  $[1\bar{1}\bar{2}]$  direction of the BaF<sub>2</sub> substrate. The hundred times weaker secondary peaks at the intermediate azimuthal directions denoted by “B”, correspond to twinned domains rotated by  $180^\circ$ .

$[1\bar{1}\bar{2}]$  surface direction of the (111) BaF<sub>2</sub> substrate. Evidently, for both samples the main layer peaks denoted by “A” appear at azimuthal angles  $\phi = 0^\circ$ ,  $120^\circ$ ,  $240^\circ$ , and  $360^\circ$ , indicating that the  $[1\bar{1}00]$  direction of the hexagonal layer lattice is parallel to the  $[1\bar{1}\bar{2}]$  substrate direction. The appearance of equivalent peaks in azimuthal directions differing by  $120^\circ$  is in agreement with the 3-fold  $R\bar{3}m$  symmetry of the BiTe and Bi<sub>2</sub>Te<sub>3</sub> lattice structures. However, the azimuthal scans also show weak additional secondary peaks denoted by “B” at azimuthal positions of  $60^\circ$ ,  $180^\circ$  and  $300^\circ$ , indicating the presence of a small number of twinned domains for which the  $[1\bar{1}00]$

direction is antiparallel to the  $[11\bar{2}]$  substrate direction, that is, the domain lattice is rotated by  $180^\circ$ . Reciprocal space maps measured in the vicinity of the secondary domain peaks show that the peak widths do not differ from those of the untwinned domains, i.e., the coherent size and rms misorientation is the same as that of the untwinned ones. Moreover, the intensity ratio of the twinned peaks does not show any dependence on the epilayer thickness. This indicates that the formation of the secondary twin domains occurs already in the early nucleation stage of growth. Since the intensity of the twinned domain peaks is only about 1/100 of the untwinned ones, the probability of twin formation on  $\text{BaF}_2$  (111) is very low for both  $\text{Bi}_2\text{Te}_3$  and  $\text{BiTe}$  epilayers, which is contrary to the growth on  $\text{Si}$  (111) where a much higher twinning ratio was reported.<sup>19</sup> This is another indication for the superior quality of our layers.

**Raman Scattering.** For further assessment of the layer properties, Raman spectra were measured in the backscattering geometry both from the front side as well as back side of the layers through the transparent  $\text{BaF}_2$  substrate. The penetration depth of the exciting 632.8 nm HeNe laser light was obtained from ellipsometric measurements and amounts to about 28 nm for  $\text{Bi}_2\text{Te}_3$  and 25 nm for  $\text{BiTe}$ . The back side and front side Raman spectra of the 830 nm  $\text{Bi}_2\text{Te}_3$  epilayer are shown in Figure 6a and b, respectively. Very similar spectra were measured at different spots of the sample as well as on the

layer with smaller thickness. The Raman spectra show three strong bands, corresponding to the normal modes of A and E symmetry.<sup>46</sup> The peaks were fitted by convolution of Gaussian and Lorentzian lineshapes represented by the dashed lines in Figure 6a using an additional weak linear background. Evidently, the model spectra are in excellent agreement with the measured spectra, that is, the difference between the experimental and fitted spectra (open squares in Figure 6a) is very small and indicates only a slight asymmetry of the bands.

The frequencies and widths (fwhm) of the two  $A_g$  and one  $E_g$  vibrations of  $\text{Bi}_2\text{Te}_3$  obtained from the fits of several independent measurements on different position and samples are listed in Table 2, together with literature values, correcting

**Table 2. Measured Raman Frequencies and Widths (fwhm) of the  $\text{Bi}_2\text{Te}_3$  Epilayers in Units of  $\text{cm}^{-1}$  Derived from Figure 6 and Their Comparison with Literature Values from Epilayers,<sup>26,25</sup> Bulk Crystals,<sup>46,47</sup> as well as Microcrystals<sup>48</sup>**

$\text{Bi}_2\text{Te}_3$	sample type	$A_{1g}^1/\text{fwhm}$	$E_g^2/\text{fwhm}$	$A_{1g}^2/\text{fwhm}$
front side	epilayers/ $\text{BaF}_2$	60.9/3.0	101.2/3.7	133/9
back side	epilayers/ $\text{BaF}_2$	60.6/3.1	100.8/4.0	133/10
ref 26	epilayer/ $\text{GaAs}$	—/—	102/—	134/—
ref 25	epilayer/ $\text{GaAs}$	—/—	99.8/—	132/—
ref 46	bulk	62.5/—	103/—	134/—
ref 47	bulk	62.0/5	102.3/6	134/10
ref 48	microcrystals	61/3.5	101/4.5	133/—

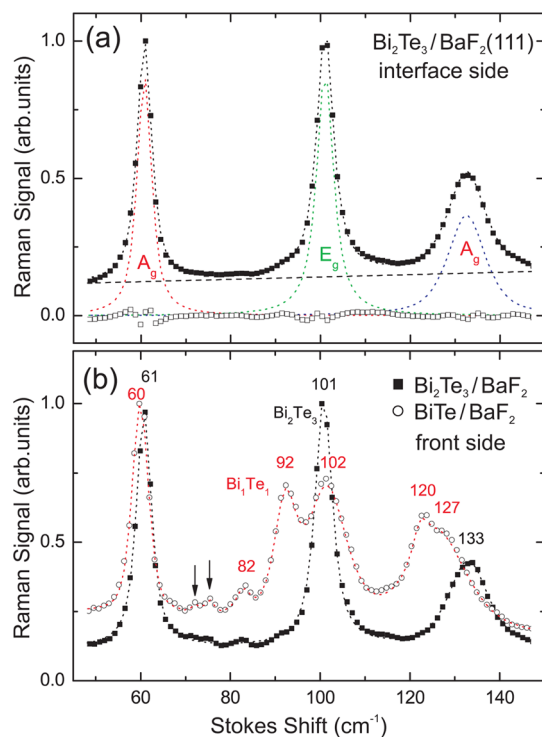


**Figure 6.** (a) Backside Raman spectrum (full squares) of the 830 nm  $\text{Bi}_2\text{Te}_3$  epilayer measured through the transparent  $\text{BaF}_2$  substrate from the  $\text{Bi}_2\text{Te}_3/\text{BaF}_2$  interface. The dashed lines represent the deconvolution of the spectrum by the sum of three Gauss-Lorentzians and a linear background. The difference between measured and model spectra is represented by the open squares. (b) Front side Raman spectra of the  $\text{Bi}_2\text{Te}_3$  (squares) and the 400 nm  $\text{BiTe}$  (open circles) epilayer. The dashed lines represent the model fits and the detected peak positions are labeled by the red and black numbers in units of  $\text{cm}^{-1}$ . The weak Raman bands highlighted by the arrows are attributed to surface oxidation.

for the  $1.5 \text{ cm}^{-1}$ -wide Gaussian profile of our instrument. The small fwhm values confirm the excellent quality of our epilayers. Identical Raman spectra, i.e., peak positions and fwhm values were obtained from the front side and back side of the layers (see Table 2 and Figure 6b and a). This demonstrates that the epilayers are highly uniform in strain and composition both in the lateral as well as vertical direction and that the lattice perfection is already very high at the layer/substrate interface. This is a clear indication for pseudomorphic growth because of the near-perfect substrate lattice-matching. The only minor difference is the appearance of very weak additional bands in the front side Raman spectra, such as those labeled by arrows in Figure 6b, which we attribute to surface degradation in humid air and are not present in the Raman spectra collected from the backside from the layer/substrate interface. Detailed studies on the oxidation process of  $\text{Bi}_2\text{Te}_3$  and  $\text{Bi}_2\text{Se}_3$  have been presented elsewhere.<sup>49</sup>

Raman measurements were also performed for the  $\text{BiTe}$  epilayers and the result is shown in Figure 6b by the open circles. All  $\text{BiTe}$  samples exhibit six pronounced bands above  $50 \text{ cm}^{-1}$ , with slightly larger widths when excited through the substrate side. The latter is a signature of the less good lattice matching to the substrate in this case. Table 3 lists the frequencies and widths obtained from the fit of the Raman spectra, together with the only reported literature data obtained from a polycrystalline  $\text{BiTe}$  film grown by pulsed laser deposition (PLD) on silicon substrate.<sup>31</sup> Since 12 different Raman-active bands are expected for the rather complex  $\text{BiTe}$  structure<sup>31</sup> in a fairly narrow frequency interval, the relatively small widths of the Raman peaks of our samples (see Table 3) confirm the high quality of the layers found by our x-ray studies. The additional weak features at  $72$  and  $75 \text{ cm}^{-1}$  of variable strength in the spectrum from the film surface (arrows in Figure 6b) are again attributed to surface oxidation.

**Table 3.** Measured Raman Frequencies and Widths (fwhm) of the Bi<sub>1</sub>Te<sub>1</sub> Epilayers in Units of cm<sup>-1</sup> Derived from Figure 6b Compared to Literature Values Obtained for Polycrystalline Pulsed Laser Deposited (PLD) Films<sup>31</sup>

BiTe	sample type	$\nu$ /fwhm					
front side	epilayers/BaF <sub>2</sub>	60.0/3.3	83/2.8	92.3/4.7	101.6/9	122/6	128/7
back side	epilayers/BaF <sub>2</sub>	59.0/4.5	83/10	90.8/6	101.9/11	120/7	126/17
ref 31	PLD films			88/–		117/–	

**Optical and Electronic Properties.** The optical constants of the Bi<sub>2</sub>Te<sub>3</sub> and BiTe epilayers were determined over a wide spectral range from the far-infrared to the ultraviolet (UV), combining spectroscopic ellipsometry and reflectivity measurements including synchrotron data acquired at NLS Brookhaven. The near-normal incidence infrared reflectivity was analyzed with the standard model of coherent interferences within a layer on a substrate,<sup>50</sup> assuming the dielectric function of the layer in the Drude-Lorentz form as described in detail in the Supporting Information.

Figures 7a and b show the real part of the optical conductivity  $\sigma_1(\omega) = -i\omega\epsilon_0(\epsilon(\omega) - 1)$  derived for the BiTe

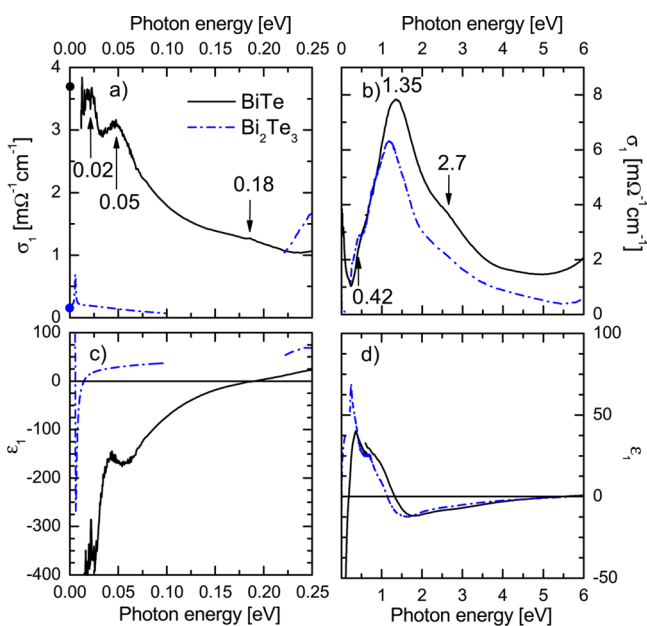


**Figure 7.** Real part of conductivity (top) and real part of the dielectric function (bottom) of BiTe (black solid lines) and of Bi<sub>2</sub>Te<sub>3</sub> (blue dash-dotted lines) added for comparison. For clarity the spectra for the far-infrared (left) and near-infrared–ultraviolet ranges (right) are displayed on different scales. The dots in panel a correspond to the measured dc conductivity measured in van der Pauw geometry.

(black solid lines) and Bi<sub>2</sub>Te<sub>3</sub> epilayers (blue dash-dotted lines), and Figure 7c and d the real part of the dielectric function  $\epsilon_1(\omega)$ . The dispersion of the optical constants was obtained by the combination of reflectivity in the far-infrared, and ellipsometry at higher frequencies, using the variational dielectric function approach.<sup>51</sup> The Bi<sub>2</sub>Te<sub>3</sub> sample is transparent in the energy range below about 0.2 eV and from the resulting interference fringes the layer thickness was determined as 830 nm. The BiTe epilayer is only slightly transparent below 0.2 eV because of much stronger free carrier absorption. The corresponding thickness was obtained as (390 ± 5) nm close to the nominal value of 400 nm. The derived pseudodielectric function of Bi<sub>2</sub>Te<sub>3</sub> in the 0.6–6 eV range did not exhibit any detectable angular dependence. Consequently,

it represents the in-plane response  $\vec{E} \perp c$ . At these photon energies the reported anisotropy of bulk Bi<sub>2</sub>Te<sub>3</sub> is small.<sup>52</sup> The characteristic energies of the spectral features seen in Figure 7b are in good agreement with those of bulk Bi<sub>2</sub>Te<sub>3</sub> reported in ref 52.

For BiTe, the absorption above 0.3 eV is due to interband transitions, dominated by the strong band at 1.35 eV, and side bands at 0.42 and 2.7 eV as indicated by the arrows in Figure 7b. This structure is similar to that of Bi<sub>2</sub>Te<sub>3</sub>, which is represented by the blue dash-dotted line for comparison. The interband transitions are likely related to the Bi–Te bilayer, which is the basic building block of both the Bi<sub>2</sub>Te<sub>3</sub> and BiTe structure (see Figure 1). The weaker band at 0.18 eV in BiTe (see Figure 7a) is related to the 0.15 eV structure in Bi<sub>2</sub>Te<sub>3</sub> reported in ref 52. At lower energies, the increase of the real part of conductivity and the decrease of the real part of the dielectric function with the decreasing photon frequency arises from the strong contribution of conducting electrons. The analysis of the spectra using the Drude model yields  $\omega_{\text{pl}} = 1.58 \pm 0.04$  eV and  $\gamma = 0.09 \pm 0.01$  eV. Using

$$\omega_{\text{pl}}^2 = \frac{nq^2}{m^*\epsilon_0} \quad (1)$$

where  $n$  is the carrier concentration and  $q$  and  $m^*$  the charge and effective mass, the free carrier concentration in BiTe is found to be about 20 times larger than in Bi<sub>2</sub>Te<sub>3</sub>, assuming the effective masses are roughly the same. Since our X-ray and Raman measurements have revealed a high crystalline perfection of the samples and no signatures of increased broadening is found in the optical spectra, this high carrier concentration in BiTe is probably not caused by extrinsic effects like vacancies but rather by a metal-like band structure, involving a band that crosses the Fermi level. This conclusion is supported by the analysis of the second BiTe sample that yielded also a large value of the plasma frequency (1.45 eV). To our knowledge, no calculations of the BiTe band structure have been available; however, calculations of the isostructural BiSe compound<sup>53</sup> show several bands crossing the Fermi level in the direction perpendicular to the  $c$ -axis, which supports our conclusion.

To confirm the large difference in the carrier concentration of the BiTe and Bi<sub>2</sub>Te<sub>3</sub> layers, we have measured the DC electric and Hall conductivities by the Van der Pauw method. The DC conductivity of BiTe amounts to  $3700 \pm 200$   $\omega^{-1}$  cm<sup>-1</sup>. The Hall effect measurement revealed n-type conductivity with a carrier concentration of  $7 \pm 1 \times 10^{20}$  cm<sup>-3</sup> using a Hall factor of unity. From this carrier concentration and the measured plasma frequency, we derive the effective electron mass to be about  $0.37 \pm 0.05 m_e$  in BiTe. Since the Hall effect measurement on the Bi<sub>2</sub>Te<sub>3</sub> samples were hampered by the Ettingshausen effect, we have measured the thermoelectric Seebeck coefficient instead, giving  $S = 170 \pm 20$  mV K<sup>-1</sup> at 300 K, which yields a free electron concentration of  $1.3 \pm 0.3 \times 10^{19}$  cm<sup>-3</sup> (see ref 54), which is more than 1 order of magnitude lower than for the BiTe epilayer, in agreement with

the optical data. The DC conductivity of  $\text{Bi}_2\text{Te}_3$  amounts to  $160 \pm 30 \omega^{-1} \text{ cm}^{-1}$ . The DC conductivities derived from the electrical measurements are indicated in Figure 7a by the black, respectively, and blue dot on the ordinate axis. Clearly, the values agree well with the low-energy extrapolation of the infrared conductivity measurements, demonstrating a good consistency of our data.

To further assess the quality of the epilayers, we have performed angle resolved photoemission (ARPES) measurement of the electronic dispersion at the UE112-PGM2a beamline of BESSY II in Berlin under ultrahigh vacuum conditions at room temperature. For protection of the samples, the surface was capped in situ after by a 100 nm Te capping layer, which was desorbed in the photoemission chamber at BESSY just before the ARPES experiments. The resulting three-dimensional band dispersion is presented in Figure 8 for

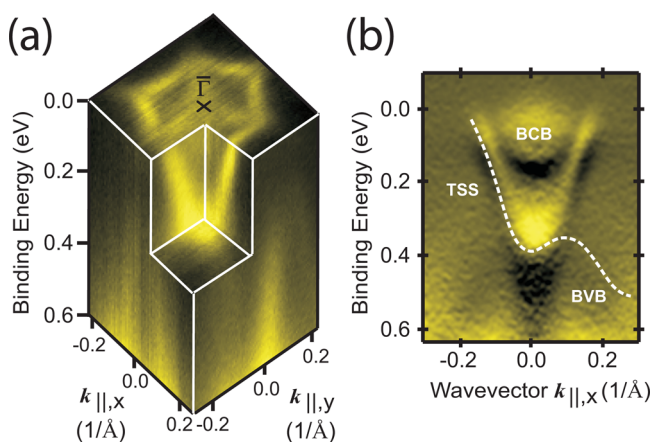


**Figure 8.** Band dispersion of the  $\text{Bi}_2\text{Te}_3$  epilayers measured by angular resolved photoemission (ARPES). Panel (a) on the left shows the three-dimensional map of the photoemission intensity in the vicinity of the  $\Gamma$  point. The Fermi level is at 0 eV, and the  $k_x$  axis corresponds to the  $\Gamma$ –K direction in the hexagonal two-dimensional surface Brillouin zone and the  $k_y$  axis to  $\Gamma$ –M direction. Panel b shows the 2D dispersion (first derivative of the photoemission intensity with respect to energy) in the  $k_x$  direction. The dashed line indicates the topologically protected surface state (TSS). BCB denotes the bulk conduction band and BVB the bulk valence band. The measurements were performed using  $\hbar\nu = 21$  eV photons for excitation.

$\text{Bi}_2\text{Te}_3$  grown under the same conditions as described above. Identical ARPES spectra were obtained from different places of the sample, indicating a high uniformity of the samples in the lateral direction. The topologically protected surface state (TSS) indicated by the dashed line in Figure 8b shows the expected linear dispersion with the Dirac point overlapping with the bulk valence band (BVB). The dispersion of the surface state deviates from the simple isotropic Dirac cone of  $\text{Bi}_2\text{Se}_3$ ,<sup>6</sup> showing a significant hexagonal warping of the band dispersion at the Fermi level, as can be seen at the top of the ARPES map displayed in Figure 8a. According to the ARPES measurements, the bottom of the bulk conduction band (BCB) lies about  $\sim 130$  meV below the Fermi level (see Figure 8b), which compares very well to the value of 120 meV calculated from the bulk electron concentration  $1.3 \times 10^{19} \text{ cm}^{-3}$ . This indicates that the free electron concentration at the surface assessed by ARPES does not differ significantly from the bulk concentration. Therefore, the Se capping and subsequent preparation of the clean surface for ARPES measurement by

annealing does not produce a charge density on the surface. The ARPES results are in nice agreement with previous theoretical and experiments on the electronic band structure of  $\text{Bi}_2\text{Te}_3$ .<sup>7</sup> This demonstrates that the structural quality of the epitaxial bismuth telluride layers is very well suited for studies of the band structure of both bulk and topological surface states. Preliminary ARPES measurements on BiTe epilayers do not show a 2D surface state, which is an indication that BiTe is not a topological insulator.

## CONCLUSION

In summary, we have demonstrated heteroepitaxial growth of different bismuth telluride phases onto  $\text{BaF}_2$  (111) substrates using molecular beam epitaxy. The stoichiometric composition of the layers was adjusted by control of the Te flux provided during growth and single phase hexagonal BiTe and  $\text{Bi}_2\text{Te}_3$  epilayers were obtained at low and high excess Te flux, respectively. The layers grow with their  $c$ -axis perpendicular to the surface and due to the good lattice matching to the  $\text{BaF}_2$  substrate, a high structural perfection was obtained. The strain, size and tilts of the coherently scattering domains were determined by high resolution X-ray reciprocal space mapping, revealing a better structural perfection of  $\text{Bi}_2\text{Te}_3$  compared to BiTe due to the almost perfect substrate lattice matching. This is supported by Raman measurements that show a low defect concentration and high crystalline quality present at the  $\text{Bi}_2\text{Te}_3/\text{BaF}_2$  interface. This suggests that the layer/substrate lattice-mismatch is an important parameter for heteroepitaxial growth of bismuth telluride epilayers, in spite of the van der Waals bonding present in the crystal structure.

For both bismuth telluride phases, the Raman modes, electronic structure, and optical properties were derived from spectroscopic measurements and the plasma frequency of free electrons as well as the interband transitions were deduced. By angular resolved photoemission spectroscopy, the three-dimensional dispersion of the topologically protected surface state was measured for  $\text{Bi}_2\text{Te}_3$  epilayers, revealing the Dirac point at the top of the bulk valence band and a strong hexagonal warping of the surface state at higher energies. The position of the Fermi level probed by photoelectron spectroscopy was found to be in good agreement with the carrier concentration in the bulk derived from transport measurements. Thus, the employed sample preparation produces very clean surfaces for photoemission studies. Infrared and transport measurements indicate a bulk metallic character of the BiTe material with a more than one order of magnitude higher carrier concentration as compared to  $\text{Bi}_2\text{Te}_3$ . To the best of our knowledge, the growth of epitaxial layers and infrared optical measurements of the BiTe phase was demonstrated for the first time. The small lattice mismatch between BiTe and  $\text{Bi}_2\text{Te}_3$  provides good conditions for fabrication of heterostructures and superlattices of the two phases. This may open a new pathway for realization of topological insulator structures.

## ASSOCIATED CONTENT

### Supporting Information

Additional information and figures showing optical properties, This material is available free of charge via the Internet at <http://pubs.acs.org>.

## AUTHOR INFORMATION

### Corresponding Author

\*E-mail: [gunther.springholz@jku.at](mailto:gunther.springholz@jku.at).

## Funding

The work was supported by the CSF grant P204/12/0595. Use of the National Synchrotron Light Source, Brookhaven National Laboratory, was supported by the U.S. Department of Energy, Office of Science, Office of Basic Energy Sciences, under Contract No. DE-AC02-98CH10886. Near-IR-VIS ellipsometry measurements at the Center for Functional Nanomaterials, Brookhaven National Laboratory, have been supported by DOE DE-AC02-98CH10886.

## Notes

The authors declare no competing financial interest.

## REFERENCES

- (1) Hasan, M. Z.; Kane, C. L. *Rev. Mod. Phys.* **2010**, *82*, 3045.
- (2) Zhang, H.; Liu, C.; Qi, X.; Dai, X.; Fang, Z.; Zhang, S. *Nat. Phys.* **2009**, *5*, 438.
- (3) Hsieh, D.; Xia, Y.; Qian, D.; Wray, L.; Meier, F.; Dil, J.; Osterwalder, J.; Patthey, L.; Fedorov, A.; Lin, H.; et al. *Phys. Rev. Lett.* **2009**, *103*, 146401.
- (4) Qu, D.; Hor, Y.; Xiong, J.; Cava, R.; Ong, N. *Science* **2010**, *329*, 821.
- (5) Qi, X.-L.; Zhang, S.-C. *Rev. Mod. Phys.* **2011**, *83*, 1057.
- (6) Xia, Y.; Wray, L.; Qian, D.; Hsieh, D.; Pal, A.; Lin, H.; Bansil, A.; Grauer, D.; Hor, Y.; Cava, R.; et al. *Nat. Phys.* **2009**, *5*, 398.
- (7) Chen, Y. L.; Analytis, J. G.; Chu, J.-H.; Liu, Z. K.; Mo, S.-K.; Qi, X. L.; Zhang, H. J.; Lu, D. H.; Dai, X.; Fang, Z.; et al. *Science* **2009**, *325*, 178.
- (8) Roushan, P.; Seo, J.; Parker, C. V.; Hor, Y. S.; Hsieh, D.; Qian, D.; Richardella, A.; Hasan, M. Z.; Cava, R. J.; Yazdani, A. *Nature* **2009**, *460*, 1106.
- (9) Moore, J. E. *Nature* **2010**, *464*, 194.
- (10) Alpichshev, Z.; Analytis, J. G.; Chu, J. H.; Fisher, I. R.; Chen, Y. L.; Shen, Z. X.; Fang, A.; Kapitulnik, A. *Phys. Rev. Lett.* **2010**, *104*, 016401.
- (11) Zhang, T.; Cheng, P.; Chen, X.; Jia, J.-F.; Ma, X.; He, K.; Wang, L.; Zhang, H.; Dai, X.; Xie, Z. F. X.; et al. *Phys. Rev. Lett.* **2009**, *103*, 266803.
- (12) Tritt, T. *Science* **1999**, *283*, 804.
- (13) Snyder, G. J.; Toberer, E. S. *Nat. Mater.* **2008**, *7*, 195.
- (14) Hsieh, D.; Xia, Y.; Qian, D.; Wray, L.; Dil, J. H.; Meier, F.; Osterwalder, J.; Patthey, L.; Checkelsky, J. G.; Ong, N. P.; et al. *Nature* **2009**, *460*, 1101.
- (15) He, L.; Kou, X.; Wang, K. L. *Phys. Status Solidi RRL* **2013**, *7*, 50.
- (16) He, X.; Guan, T.; Wang, X.; Feng, B.; Cheng, P.; Chen, L.; Li, Y.; Wu, K. *Appl. Phys. Lett.* **2012**, *101*, 123111.
- (17) Liu, H. W.; Yuan, H. T.; Fukui, N.; Zhang, L.; Jia, J. F.; Iwasa, Y.; Chen, M. W.; Hashizume, T.; Sakurai, T.; Xue, Q. K. *Cryst. Growth Design* **2010**, *10*, 4491.
- (18) Chen, X.; Ma, X.-C.; Jia, J.-F.; Xue, Q.-K. *Adv. Mater.* **2011**, *23*, 1162.
- (19) Krumrain, J.; Mussler, G.; Borisova, S.; Stoica, T.; Plucinski, L. J. *Cryst. Growth* **2011**, *324*, 115.
- (20) Borisova, S.; Krumrain, J.; Luysberg, M.; Mussler, G.; Grutzmacher, D. *Cryst. Growth Design* **2012**, *12*, 6098.
- (21) Fukui, N.; Hirahara, T.; Shirasawa, T.; Takahashi, T.; Kobayashi, K.; Hasegawa, S. *Phys. Rev. B* **2012**, *85*, 115426.
- (22) Li, Y.-Y.; Wang, G.; Zhu, X.-G.; Liu, M.-H.; Ye, C.; Chen, X.; Wang, Y.-Y.; He, K.; Wang, L.-L.; Ma, X.-C.; et al. *Adv. Mater.* **2010**, *22*, 4002.
- (23) Plucinski, L.; Mussler, G.; Krumrain, J.; Herdt, A.; Suga, S.; Grutzmacher, D.; Schneider, C. M. *Appl. Phys. Lett.* **2011**, *98*, 222503.
- (24) Zhang, S. X.; Yan, L.; Qi, J.; Zhuo, M.; Wang, Y.-Q.; Prasankumar, R.; Jia, Q.; Picraux, S. *Thin Solid Films* **2012**, *21*, 6459.
- (25) Cao, H.; Venkatasubramanian, R.; Liu, C.; Pierce, J.; Yang, H.; Hasan, M. Z.; Wu, Y.; Chen, Y. P. *Appl. Phys. Lett.* **2012**, *101*, 132104.
- (26) Liu, X.; Smith, D. J.; Fan, J.; Zhang, Y.-H.; Cao, H.; Chen, Y. P.; Leiner, J.; Kirby, B. J.; Dobrowolska, M.; Furdyna, J. K. *Appl. Phys. Lett.* **2011**, *99*, 171903.
- (27) Massalski, T. B.; Okamoto, H. *Binary Alloy Phase Diagrams*; ASM International: Materials Park, OH, 1996.
- (28) Kim, Y.; Cho, S.; DiVenere, A.; Wong, G. K. L.; Ketterson, J. B. *Phys. Rev. B* **2001**, *63*, 155306.
- (29) Bos, J. W. G.; Zandbergen, H. W.; Lee, M.-H.; Ong, N. P.; Cava, R. J. *Phys. Rev. B* **2007**, *75*, 195203.
- (30) Yamana, K.; Kihara, K.; Matsumoto, T. *Acta Crystallogr. B* **1979**, *35*, 147.
- (31) Russo, V.; Bailini, A.; Zamboni, M.; Passoni, M.; Conti, C.; Casari, C. S.; Bassi, A. L.; Bottani, C. E. *J. Raman Spectrosc.* **2008**, *39*, 205.
- (32) Peranio, N.; Eibl, O.; Nurnus, J. *J. Appl. Phys.* **2006**, *100*, 114306.
- (33) Madelung, O. *Semiconductors: Data Handbook*; Springer-Verlag: Berlin, 2004.
- (34) Wyckoff, R. W. G. *Crystal Structures*, Vol. 2; Wiley, New York, 1964.
- (35) Nakajima, S. *J. Phys. Chem. Sol.* **1963**, *24*, 479.
- (36) *Natl. Bur. Stand. (U.S.) Monogr.* **1964**, *253*, 16.
- (37) Shimazaki, H.; Ozawa, T. *Am. Mineral.* **1978**, *63*, 1162.
- (38) Stasova, M. M.; Struk, Zh. *Khim* **1967**, *8*, 655.
- (39) Hayes, W. *Crystals with Fluoride Structure*; Clarendon: Oxford, U.K., 1974.
- (40) Teweldebrhan, D.; Goyal, V.; Balandin, A. A. *Nano Lett.* **2010**, *10*, 1209.
- (41) Pietsch, U.; Holý, V.; Baumbach, T. *High-Resolution X-Ray Scattering From Thin Films to Lateral Nanostructures*; Springer-Verlag: Berlin, 2004.
- (42) Holý, V.; Kuběna, J.; Abramof, E.; Lischka, K.; Pesek, A.; Koppensteiner, E. *J. Appl. Phys.* **1993**, *74*, 1736.
- (43) Tarakina, N. V.; Schreyeck, S.; Borzenko, T.; Schumacher, C.; Karczewski, G.; Brunner, K.; Gould, C.; Buhmann, H.; Molenkamp, L. W. *Cryst. Res. Design* **2012**, *12*, 1913.
- (44) Schreyeck, S.; Tarakina, N. V.; Karczewski, G.; Schumacher, C.; Borzenko, T.; Brüne, C.; Buhmann, H.; Gould, C.; Brunner, K.; Molenkamp, L. W. *Appl. Phys. Lett.* **2013**, *102*, 041914.
- (45) Jenkins, J. O.; Rayne, J. A.; Ure, J. R. W. *Phys. Rev. B* **1972**, *3*, 3171.
- (46) Richter, W.; Kohler, H.; Becker, C. *Phys. Status Solidi B* **1977**, *84*, 619.
- (47) Kullmann, W.; Geurts, J.; Richter, W.; Lehner, N.; Rauh, H.; Steigenberger, U.; Eichhorn, G.; Geick, R. *Phys. Status Solidi B* **1984**, *125*, 131.
- (48) Atuchin, V.; Gavrilova, T.; Kokh, K.; Kuratieva, N.; Pervukhina, N.; Surovtsev, N. *Solid State Commun.* **2012**, *152*, 1119.
- (49) Yashina, L. V.; Sánchez-Barriga, J.; Scholz, M. R.; Volykhov, A. A.; Sirotnina, A. P.; Neudachina, V. S.; Tamm, M. E.; Varykhalov, A.; Marchenko, D.; Springholz, G.; Bauer, G.; Knop-Gericke, A.; Rader, O. *ACS Nano* **2013**, *7*, 5181.
- (50) Azzam, R. M. A.; Bashara, N. M. *Ellipsometry and Polarized Light*; Elsevier Science Publisher: Amsterdam, 1987.
- (51) Kuzmenko, A. B. *Rev. Sci. Instrum.* **2005**, *76*, 083108.
- (52) Greenaway, D. L.; Harbeke, G. *J. Phys. Chem. Solids* **1965**, *26*, 1585.
- (53) Gaudin, E.; Jobic, S.; Evain, M.; Brec, R.; Rouxel, J. *Mater. Res. Bull.* **1995**, *30*, 549.
- (54) Mishra, S. K.; Satpathy, S.; Jepsen, O. *J. Phys.: Condens. Matter* **1997**, *9*, 461.